Applied Clay Science 185 (2020) 105420

Contents lists available at ScienceDirect

Applied Clay Science

journal homepage: www.elsevier.com/locate/clay

Research Paper

A novel multifunctional adsorbent synthesized by modifying acidified organo-montmorillonite with iron hydroxides

Yixuan Yang[a,b,c], Runliang Zhu[a,b,c,*], Qingze Chen[a,b,c], Haoyang Fu[a,b,c], Qiuzhi He[a,b,c], Jianxi Zhu[a,b,c], Hongping He[a,b,c]

[a] CAS Key Laboratory of Mineralogy and Metallogeny/Guangdong Provincial Key Laboratory of Mineral Physics and Materials, Guangzhou Institute of Geochemistry, Chinese Academy of Sciences, Guangzhou 510640, China
[b] University of Chinese Academy of Sciences, Beijing 100049, China
[c] Institutions of Earth Science, Chinese Academy of Sciences, Beijing 100029, China

ARTICLE INFO

Keywords:
Multifunctional adsorbent
Montmorillonite
Acid activation
Porous nanosilica
Co-adsorption

ABSTRACT

Multifunctional adsorbents based on montmorillonite (Mt) have been of highly concerns due to their unique 2D layer structures and impressive co-adsorption performances. To further enhance the support ability and reactivity, a strategy was developed in this study to enable the co-existence of porous nanosilica (PNS) and hydrophobic interlayer spaces in Mt structure, and a novel multifunctional adsorbent (iron modified-acidified organo-Mt, Fe-AOMt) was then synthesized, aiming to simultaneously remove hydrophobic contaminants, oxyanion contaminants and heavy metals in water. The combination of XRD, FTIR and TEM verified the co-existence of amorphous PNS and layered structure (containing intercalated surfactant) in the acidified organo-Mt (AOMt), and results of STEM-EDX revealed uniform distribution of Fe after the further introduction of Fe hydroxides to AOMt. Additionally, pore structure analyses suggested that the acid activation can obviously increase the pore volume and specific surface area of OMt. Batch adsorption experiments revealed that Fe-AOMt as a promising multifunctional adsorbent was able to effectively and simultaneously remove nitrobenzene, phosphate, and Cd(II) in the multi-contaminant system. The synergetic adsorption of phosphate and Cd(II) on Fe-AOMt suggested the formation of ternary surface complexes (≡Fe–P–Cd), while the pH-independent uptake of nitrobenzene was hardly influenced by adsorption of phosphate and Cd(II), implying dissimilar adsorption mechanisms. The co-adsorption mechanism on Fe-AOMt was further revealed via XPS. Our work provided a novel and efficient Mt-based multifunctional adsorbent with a newly-proposed structure, which was a preliminary exploration of diversifying locations and types of active sites in Mt structure.

1. Introduction

As a side effect of industrialization, hydrophobic organic contaminants (HOCs, e.g., nitrobenzene), oxyanion contaminants (e.g., phosphate) and heavy metal cations (e.g., cadmium(II)) emerge simultaneously in water environment (Zhu et al., 2009b; Shen and Chen, 2015; Liu et al., 2017). Since water quality must conform to stricter regulations came up in recent years, more effective and economical control of these co-existing contaminants in low concentrations is pressingly needed. Adsorption has been considered as an effective method for removing multiple contaminants in low concentrations from water. However, an adsorbent with single functional group is often effective towards the same type of contaminants, and shows unsatisfactory performance in removing multiple contaminants (Bhattacharyya and Gupta, 2008; Goh et al., 2008). Thus, multifunctional adsorbents are drawing increasing attention nowadays and composite adsorbents have been synthesized based on a variety of precursors such as activated carbon, graphene, biochar, layered double hydroxides (LDH), MoS_2 and MXene (Huang et al., 2017; Li et al., 2018; Tang et al., 2015; Dou et al., 2019; Lei et al., 2019; Rahmi et al., 2019). However, the high cost of the starting materials, complexity and/or production of hazards in synthesis may limit their utilizations. Therefore, researches have been continued on inexpensive alternatives having reasonable adsorption efficiencies (Duman et al., 2015a; Zhu et al., 2016).

Montmorillonite (Mt) is a readily available clay mineral of

* Corresponding author at: CAS Key Laboratory of Mineralogy and Metallogeny/Guangdong Provincial Key Laboratory of Mineral Physics and Materials, Guangzhou Institute of Geochemistry, Chinese Academy of Sciences, Guangzhou 510640, China.
E-mail address: zhurl@gig.ac.cn (R. Zhu).

https://doi.org/10.1016/j.clay.2019.105420
Received 21 September 2019; Received in revised form 19 December 2019; Accepted 23 December 2019
Available online 07 January 2020
0169-1317/

considerable reserve. As a layered silicate of 2:1 type, Mt receives growing attention owing to its natural nanostructure, i.e., a two-dimensional (2D) nanosheet-shaped layered structure featuring diverse morphological advantages, such as high specific surface area, abundant active sites and possession of interlayer space for hybridization with different species (Low et al., 2014; Zhang et al., 2014). The interlayer space of Mt is easily accessible due to the exchangeable cations contained therein, which is resulted from the positive charge deficiency of its layer (Bhattacharyya and Gupta, 2008). Because of its unique structure, low cost, natural abundance, and environment friendliness, Mt has been used as precursor to synthesize varied adsorbents, including the multifunctional adsorbents for removing multiple contaminants from water (Liu et al., 2016a, 2016b; Ma et al., 2016a, 2016b). For example, inorganic-organic Mt, a typical multifunctional adsorbent, can be synthesized through intercalating both inorganic and organic species into the interlayer spaces of Mt. The resulting materials can adsorb both inorganic and organic contaminants simultaneously (Ma and Zhu, 2006; Zhu et al., 2009b; Ma et al., 2016c). However, such strategy to multi-functionalize Mt can limit the support ability and reactivity of its interlayer spaces and therefore restricts its performance. Firstly, active sites in the interlayer spaces may be insufficient when shared by different intercalated agents. Secondly, inorganic species can exert “lock effect” in the interlayer spaces, which will constrain the intercalation of surfactants (Zhu et al., 2009a). Thus, to optimize the multifunctional modification, new strategies are needed to expand the spaces and active sites in Mt structure for enhancing the support ability and reactivity.

Early studies revealed that acid activation is a facile way to modify the silicate layers of clay minerals (Komadel and Madejová, 2013; Komadel, 2016). By complete acid leaching of their octahedral (O) sheets, the silicon–oxygen tetrahedral (T) layers, which lacks functional groups on their surfaces (Bhattacharyya and Gupta, 2008), can transform into amorphous porous nanosilica (PNS) products with considerable surface hydroxyl groups and enhanced pore structure (Wang et al., 2016; Pentrák et al., 2018; Chen et al., 2019). Wang et al. (2012, 2013, 2016, 2019) have done a lot of works on the acidified clay minerals, and proved the derived PNS to be an excellent precursor material, which possesses considerable advantages such as the capacity of effectively anchoring and dispersing reactive nanoparticles. By simply controlling the acidification conditions, products with PNS and original interlayer spaces co-existing in different ratios can be acquired (Steudel et al., 2009; Pentrák et al., 2018). Herein, we envision that if the support ability and reactivity of interlayer spaces can be retained along with the creation of PNS (i.e., in the acidification process of Mt), the obtained material would be endowed with enhanced performance. However, the generation of PNS and the preservation of original interlayer spaces is mutually exclusive, since the dissolution of O sheets will result in loss of cation exchange capacity (CEC) of the interlayer spaces. No study has been reported, to the best of our knowledge, to create PNS and retain the interlayer spaces simultaneously and effectively in Mt structure.

Hence, we developed a new strategy to multi-functionalize Mt and synthesized a novel multifunctional adsorbent. The route of synthesizing the adsorbent and its co-adsorptive ability was illustrated schematically in Scheme 1. First, organo-Mt (OMt) was prepared by intercalating cetyltrimethylammonium cations ($CTMA^+$) into Mt, which can form partition media in the interlayer spaces for sorption of HOCs. OMt was then acidified with concentrated nitric acid to produce acid-activated OMt (AOMt). Considering the hydrophobic interaction between the long alkyl chains of $CTMA^+$ (Madejová et al., 2009; Tomić et al., 2012), most of $CTMA^+$ were expected to be retained when the CEC was reduced. Meanwhile, massive PNS was envisioned to be generated during the acidification process, being effective in loading of metal hydroxides. Finally, Fe hydroxides, which can provide the affinity towards phosphate and heavy metals (Ma and Zhu, 2006; Zhu et al., 2014b; Ma et al., 2016b), were introduced to AOMt. The resulting material, denoted as Fe-AOMt, should be able to remove HOCs, oxyanion contaminants, and heavy metal cations simultaneously and effectively from water. Thus, the structural characteristics of Fe-AOMt and its co-adsorptive behaviors towards nitrobenzene, phosphate, and Cd (II) were investigated.

2. Materials and methods

2.1. Chemicals

Mt with purity above 95% was obtained from Inner Mongolia, China. The main chemical composition of Mt was investigated by X-ray fluorescence (XRF), and the result was reported in Table S1. The CEC of Mt was 114 mmol/100 g. Cetyltrimethylammonium bromide (CTMAB, $C_{16}H_{33}(CH_3)_3NBr$), nitrobenzene ($C_6H_5NO_2$) and sodium dihydrogen phosphate (NaH_2PO_4) were purchased from Macklin. Cadmium nitrate ($Cd(NO_3)_2{\cdot}4H_2O$) was purchased from Aladdin. Ferric nitrate ($Fe(NO_3)_3{\cdot}9H_2O$) was purchased from Tianjin Damao Chemical Reagent Factory, China. Sodium hydroxide (NaOH) and nitric acid (HNO_3) were purchased from Guangzhou Chemical Reagent Factory, China. All of the reagents were of analytical grade and used as received.

2.2. Preparation of OMt, AOMt and Fe-AOMt

The Mt was used as the starting material and passed through a 200-mesh sieve (0.074 mm). First, 0.057 mol/L CTMAB was added into 100 g/L Mt suspension to achieve 50% exchange of CEC of Mt The mixture was stirred for 2 h at 60 °C and aged for another 2 h at 70 °C in a water bath to yield OMt. OMt (25 g/L) was then activated in 6 mol/L nitric acid for 3 h in a water bath at 80 °C to synthesize AOMt. The resultant AOMt was filtrated, washed with deionized (DI) water and air-dried.

To synthesize Fe-AOMt, 100 g/L AOMt was impregnated in 0.2 mol/L $Fe(NO_3)_3$ solution for 2 h to achieve ~10% of Fe loading amount. After the impregnation, pH of the suspension was adjusted to ~3.2 with dropwise addition of 4 mol/L NaOH, when the precipitates of Fe hydroxides just formed. After being aged for 12 h, the suspension was evaporated at 80 °C to produce Fe-AOMt. The solid was then washed with DI water to remove the nitrate impurities and freeze-dried.

2.3. Batch adsorption experiments

The adsorption experiments were conducted in two systems: (1) adsorption of a single contaminant, and (2) simultaneous adsorption of the three contaminants. For system #1, adsorption of each single contaminant was measured using an initial concentration of 0–100 mg/L for nitrobenzene, 0–35 mg/L for phosphate and 0–35 mg/L for Cd(II). For system #2, the concentration of each contaminant was constant: 60 mg/L for nitrobenzene and 25 mg/L for phosphate and Cd(II). The initial pH was adjusted to ~4.0 (± 0.05) using 0.1 mol/L HNO_3 or 0.1 mol/L NaOH.

The effects of pH on the adsorption on Fe-AOMt were investigated in both single- and multi-contaminant systems, in which the concentrations of contaminants were set at 60 mg/L for nitrobenzene, 25 mg/L for phosphate and Cd(II), and the initial solution pH was set in the scope of 2.5–6.

0.02 g solid was mixed with 20 mL solution in a 50 mL polypropylene tubes to investigate the adsorption performances of Fe-AOMt, AOMt and OMt. The tubes were shaken at 200 rpm for 24 h to reach equilibrium, and then the concentration of each contaminant in the suspension was determined after filtration. All experiments were carried out in triple and the error bars were displayed in the figures.

2.4. Analysis and characterization techniques

X-ray powder diffraction (XRD) data was recorded using Bruker D8

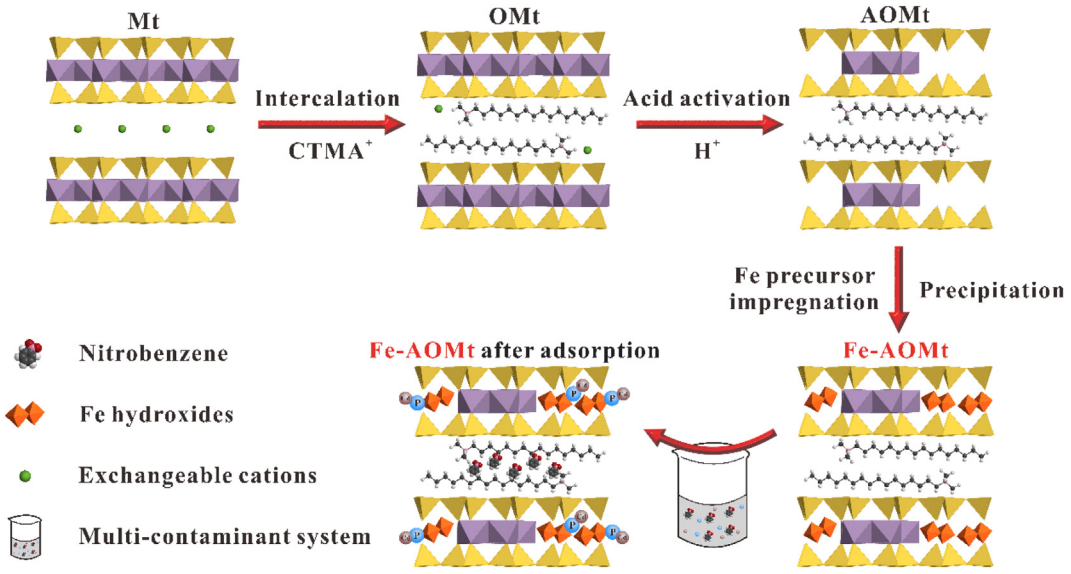

Scheme 1. The schematic illustration of the new strategy to multi-functionalize Mt, and the expected co-adsorption performance of the novel multi-functional adsorbent, Fe-AOMt towards nitrobenzene, phosphate and Cd(II).

ADVANCE X-ray diffractometer with Cu/Ka radiation (40 kV, 40 mA) in 2θ range from 3° to 80°. The amount of $CTMA^+$ in the solid was determined by total organic carbon analysis (Vario EL Cube, Elemetar). The release of Al^{3+}, Mg^{2+}, and Fe^{3+} after the acid activation of OMt was analyzed by inductively coupled plasma atomic emission spectrometry (Varian VISTA PRO ICP-AES, Agilent, USA).

Micromeritics ASAP 2020 static volumetric analyzer was applied to obtain nitrogen adsorption-desorption isotherms of the samples. The samples were degassed under vacuum at 200 °C for 12 h prior to determination. Multiple-point Brunauer-Emmett-Teller (BET) method was used to calculate their specific surface area, and adsorption points in p/p_0 range from 0.05 to 0.20 were selected. The total pore volume (V_{total}) was evaluated at $p/p_0 \approx 0.99$, and the pore size distribution analysis was determined according to the model of Non-Local Density Functional Theory (NLDFT).

The Fourier transform infrared (FTIR) spectra of the samples were recorded on a Brucker Vertex-70 FTIR spectrometer. Each specimen for FTIR detection was a translucent chip, which was prepared by pressing the mixture of 0.9 mg sample powder and 80 mg KBr.

Analyses of high-resolution transmission electron microscopy (HRTEM) and X-ray energy-dispersive spectroscopy on the mode of scanning transmission electron microscopy mode (STEM-EDX) were conducted in FEI Talos F200S HRTEM equipped with Super-X X-ray spectroscopy operating at 200 kV.

X-ray photoelectron spectroscopy (XPS) patterns were detected by a Thermo Scientific K-Alpha spectrometer equipped with Al Kα source (1486.8 eV). The spectra were collected with pass energy of 30 eV and analysis area of 400 μm^2. The C1s peak at 284.8 eV was used as reference to correct the charging effect. All data were fitted with smart background correction. The samples were collected from "P" (25 mg/L phosphate) and "Cd" system (25 mg/L Cd(II)), "NB + P" (60 mg/L nitrobenzene and 25 mg/L phosphate) and "NB + Cd" (60 mg/L nitrobenzene and 25 mg/L Cd) system, and "NB + P + Cd" system (60 mg/L nitrobenzene, 25 mg/L phosphate and 25 mg/L Cd(II)). All specimens were freeze-dried before the detection.

The concentration of phosphate was measured with the molybdenum blue method (USEPA, 1983), for which UV–*vis* spectrophotometer (UV2400, Shanghai Sunny Hengping Scientific Instrument Co., Ltd., China) was applied. Atomic absorption spectrometry (ZA3000 AAS, HITACHI, Japan) was used to determine the concentration of Cd (II). The concentration of nitrobenzene was detected by High Performance Liquid Chromatography (Agilent 1260 Infinity LC) at wavelength of 280 nm, and methanol-water mixture (70:30, *v*/v) was used as the mobile phase with flow rate set at 1 mL/min.

3. Results and discussion

3.1. Structural characteristics of adsorbents

3.1.1. Co-existence of PNS and interlayer $CTMA^+$

According to the XRD patterns presented in Fig. 1a, the basal spacing of Mt was of 1.5 nm, indicating a typical 001 plane calcium Mt (Bergaya and Lagaly, 2013). The d_{001} value of 1.7 nm for OMt suggested that the intercalated $CTMA^+$ was arranged in lateral-bilayer structure, with a loading amount of ~50% of CEC (He et al., 2006; Zhu et al., 2007). As revealed by the XRD pattern of AOMt, acid activation can change the structure of OMt. Firstly, the decrease in the diffraction intensity should be ascribed to the reduction of layer stacking and the partial transformation of OMt to amorphous silica products (Pentrák et al., 2018). Secondly, the broadened d_{001} suggested the presence of heterogeneous basal spacings of AOMt. Because of the partial exchange of Ca^{2+} by $CTMA^+$, the interlayer spaces of OMt should still contain Ca^{2+}, which would be further replaced by protons, as well as by the cations released from Mt layers (Al^{3+}, Fe^{3+}, and/or Mg^{2+}) during the acid activation process. Thus, the d_{001} of AOMt was distributed in a wider range because of the heterogeneous distribution of the different replaced cations (Breen et al., 1995; Komadel and Madejová, 2013; Komadel, 2016). On the other hand, previous studies also convinced the retaining of surfactant cations (e.g., $CTMA^+$) in the interlayer spaces of acidified organoclays (Komadel and Madejová, 2013). Indeed, the results of TOC analysis and the ICP-AES analysis of the supernatant collected from the acidification of OMt also revealed that $CTMA^+$ can be well retained on AOMt (Fig. S1). The introduction of Fe species did not alter the central position of d_{001} as well, but led to obvious drop of the intensity of all diffractions, suggesting the further decrease of the rigid layered structure of AOMt.

FTIR spectroscopy provided evidences about the change of surface functional groups after the acid activation and introduction of Fe hydroxides, as revealed by the specific signals of bond vibrations (Fig. 1b). The emerging bands of OMt at 2926 and 2854 cm^{-1} can be referred to the stretching vibration of $–CH_2$ on $CTMA^+$, and that at 1477 cm^{-1} was attributed to the bending vibration of $–CH_2$. These bands showed consistence in the patterns of AOMt and Fe-AOMt, indicating the preservation of intercalated $CTMA^+$ after acid activation and Fe

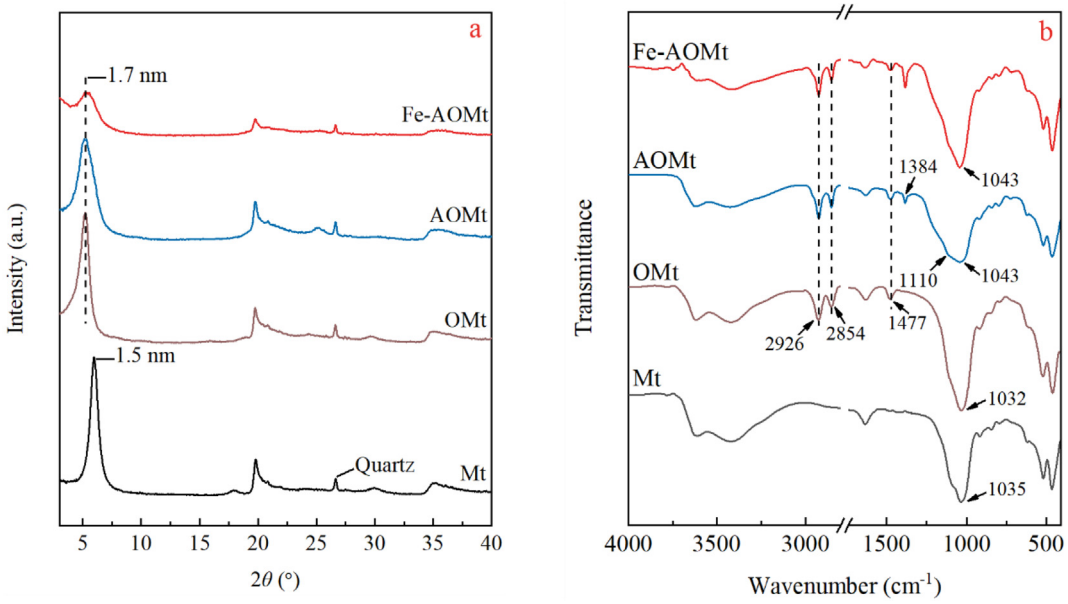

Fig. 1. (a) XRD patterns and (b) FTIR spectra of Mt, OMt, AOMt and Fe-AOMt.

introduction, which was further convinced by the results of the TOC analysis (Fig. S1). Note that in previous studies on acidified organo-Mt, relatively high loading amounts (> 1.0CEC) of surfactants were applied (Madejová et al., 2009; Tomić et al., 2012); it is rarely reported that a lower loading amount (0.5CEC, adopted in this work) can still achieve the defensive ability. It is unexpected that the characteristic bands for NO_3^- vibration at 1384 cm^{-1} appeared in the pattern of AOMt and Fe-AOMt, even after several times of washes. A possible reason is that as the loss of negative layer charges proceeds during acid activation, extra negative charges (i.e., NO_3^-) would be needed to compensate the positive charges from $CTMA^+$ and Fe hydroxides. Yuan et al. (2008) also suggested that NO_3^- could be the charge-compensating anions that coexists with the introduced Fe hydroxides within the interlayer spaces of Mt The band at ~1035 cm^{-1} for the stretching vibration of Si—O showed no obvious change in the patterns of Mt and OMt, but that of AOMt was clearly broadened by two emerging bands at ~1043 cm^{-1} and ~1110 cm^{-1}. After the introduction of Fe hydroxides, the band was located at ~1043 cm^{-1}. In previous studies about acidification process of Mt or surfactant-intercalated Mt, the shifts from ~1035 cm^{-1} to higher wavenumbers were attributed to the conversion of Si—O bond in tetrahedral sheets to that in amorphous silica products (Breen et al., 1997; Pálková et al., 2003; Madejová et al., 2009; Tomić et al., 2012). Similar shifts of other layered silicates under acid activation was also observed (Vicente Rodriguez et al., 1995; Wang et al., 2016). Broadened bands or shoulders for Si—O were also found in some studies where moderate acidification conditions were applied (Madejová et al., 1998; Pentrák et al., 2018). Thus, the acid activation was preliminarily determined to be successfully conducted with amorphous silica products generated and $CTMA^+$ kept in AOMt simultaneously.

The morphologies of OMt, AOMt and Fe-AOMt layers were detected by TEM (Fig. 2a-c). Lattice fringes was shown in Fig. 2a, implying the high crystallization of OMt, which was also convinced by the XRD pattern of OMt (Fig. 1a). Irregular morphologies were observed in AOMt (Fig. 2b), which were corresponded to the amorphous PNS created by acid activation. Similar morphologies were also observed in the PNS derived from vermiculite, another 2:1 aluminosilicate clay mineral (Wang et al., 2016). Moreover, some lattice fringes originated from OMt layer could be observed to co-exist with the PNS in AOMt and Fe-AOMt (Fig. 2a-c insets). Such morphological change was consistent with the results of XRD and FTIR results, providing evidences of the successful creation of both PNS and hydrophobic interlayer spaces via our new strategy. However, it is not easy to discriminate the morphological characteristics between the loaded Fe hydroxides and PNS in Fe-AOMt (Fig. 2c), since they were both weakly crystallized and may share similar morphologies.

3.1.2. Loading of Fe hydroxides on Fe-AOMt

The element (Fe) mappings of the three materials provided by STEM-EDX were displayed (Fig. 2d-f), and the element contents (Al, Si and Fe) of the scanned areas were also offered in the attached tables. According to the results, the Fe content of OMt was ~4% in weight (wt) (Fig. 2d), which was almost corresponded to the XRF result of raw Mt (Table S1) with the intercalation of $CTMA^+$ considered, and attributed to the Fe^{3+} in its octahedral sheets; that decreased to ~1%wt for AOMt due to the loss of octahedral Fe^{3+} during the acid activation (Fig. 2e). The distribution of Fe on Fe-AOMt (Fig. 2f) was as uniform as that of Si and Al (Fig. S2), revealed effective support of Fe hydroxides. Additionally, Fe-AOMt possessed a Fe content of ~12 wt% (Fig. 2e), which almost tallied the adding amount of Fe (~10 wt%) during the process of impregnation, suggesting the efficient utilization of the Fe precursor. In addition, the atomic ratio of Al and Si in OMt was ~1:3.5 (Fig. 2d), and dropped markedly to ~1:8 after the acid activation (Fig. 2e), implying that protons preferred to attack Al—O than Si—O bonds in OMt and caused the loss of Al^{3+} (Fig. S1b). Such mechanism was also implied by previous studies on the acid activation of Mt (Tkáč et al., 1994; Krupskaya et al., 2017; Pentrák et al., 2018).

3.1.3. Pore structures

Nitrogen adsorption-desorption isotherms and pore volume distribution of the samples were obtained (Fig. 3). Parameters of the total pore volume (V_{total}) and BET specific surface area (S_{BET}) were calculated (Table 1). All of the isotherms were of type IV with H3 hysteresis-loop, revealing a typical slit pores model of mesoporous (pore width = 2–50 nm) and macroporous (pore width > 50 nm) structures for these samples (a), and the precipitous elevation in the isotherms at low p/p_0 refers to the contribution by micropores (pore width < 2 nm). Obviously, such elevation existed in the isotherm of Mt but disappeared in that of OMt, indicating that the micropores in Mt were almost completely blocked or filled by $CTMA^+$ (He et al., 2006). In fact, modification by $CTMA^+$ caused overall shifting of pore volume from micropores to macropores (Fig. 4b). On the other hand, the acid

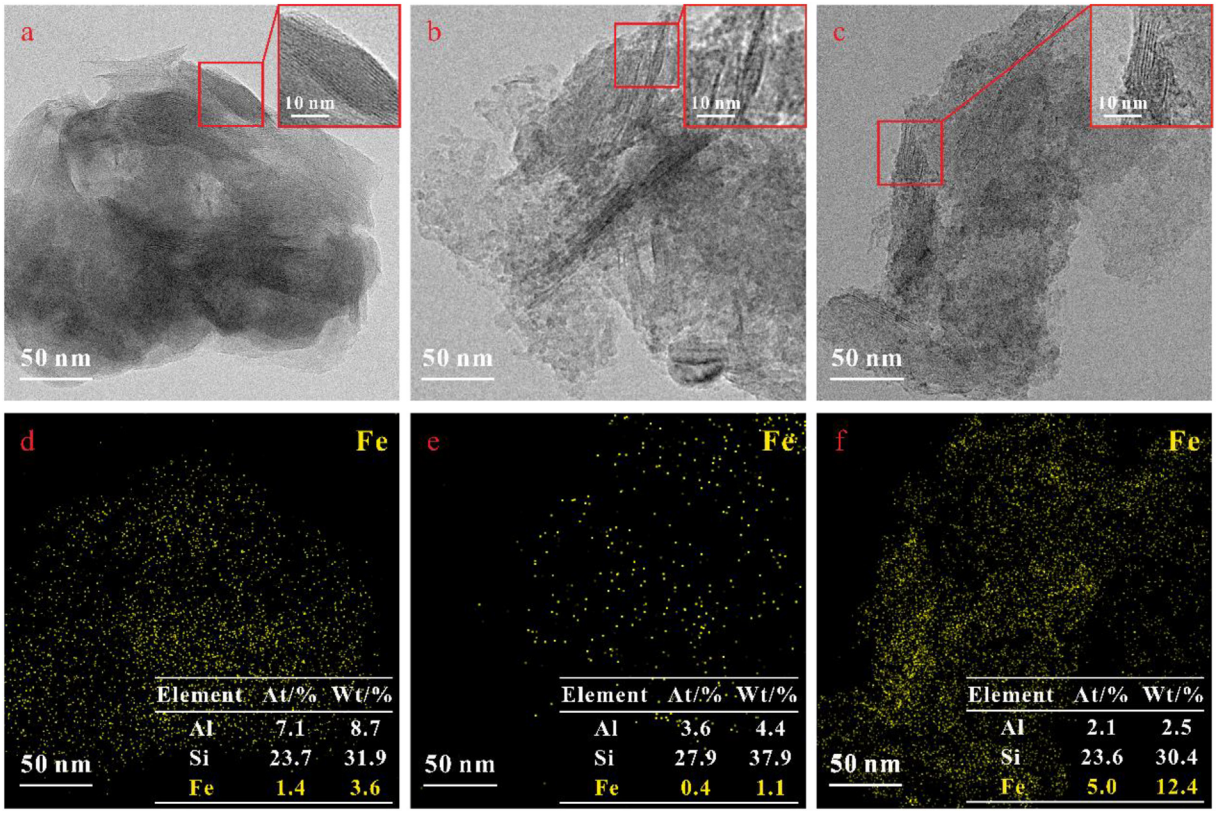

Fig. 2. TEM images of (a) OMt, (b) AOMt and (c) Fe-AOMt (insets: corresponding TEM images under higher magnification) and the corresponding STEM-EDX mapping of Fe (d) in panel a, (e) in panel b and (f) in panel c. Attached sheets in (d) to (f) offered the element contents in atomic (At.%) and mass ratio (Wt%) on the scanned area detected by STEM-EDX.

activation totally enhanced the pore volume of mesopores (Fig. 3b), and the S_{BET} and V_{total} was arisen accordingly from 18.2 m^2/g and 0.066 cm^3/g for OMt to 91.4 m^2/g and 0.201 cm^3/g for AOMt, respectively (Table 1). Such result was in good agreement with the presence of the PNS, as it was featured as a mesoporous nanosilica product (Ishii et al., 2005; Okada et al., 2010; Wang et al., 2016). The S_{BET} further increased to 117.4 m^2/g after the introduction of Fe hydroxides (Table 1), which can be attributed to their large specific surface area (Cornell and Schwertmann, 2003; Fu et al., 2018) (Fig. 3b).

According to above characterization results, the structural change from OMt to AOMt, and further the resulting Fe-AOMt can be summarized as follows. Hydrophobic interlayer spaces were preserved as the intercalated $CTMA^+$ showed strong defensive ability against the acid attack. Nevertheless, octahedral sheets of OMt layers still suffered from the acid activation with considerable loss of their structural cations. As a result, massive amorphous porous PNS was produced, co-

Table 1
BET specific surface area and total pore volume of Mt, OMt, AOMt and Fe-AOMt.

Sample	S_{BET} (m^2/g)	V_{total} (cm^3/g)
Mt	60.6	0.125
OMt	18.2	0.066
AOMt	91.4	0.201
Fe-AOMt	117.4	0.184

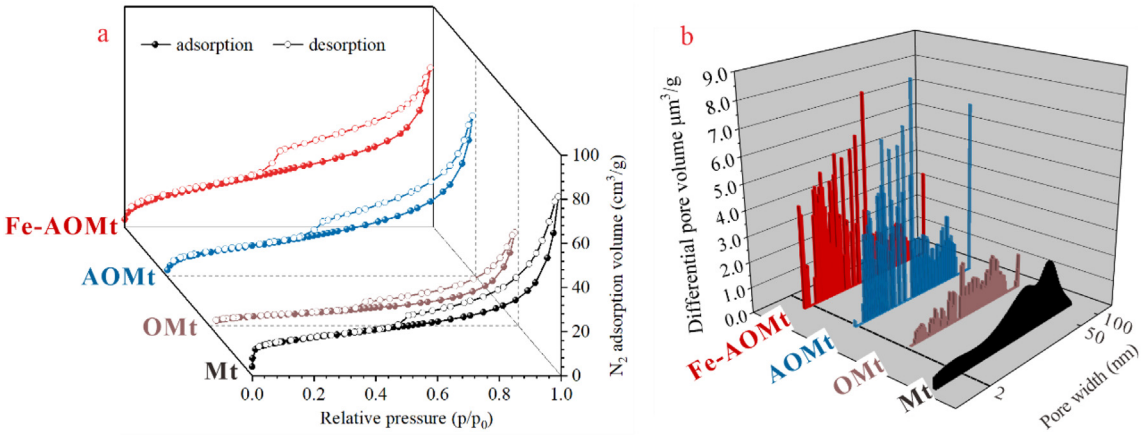

Fig. 3. (a) Nitrogen adsorption-desorption isotherms of Mt, OMt, AOMt and Fe-AOMt. (b) Pore size distribution of Mt, OMt, AOMt and Fe-AOMt calculated via the model of Non-Local Density Functional Theory (NLDFT).

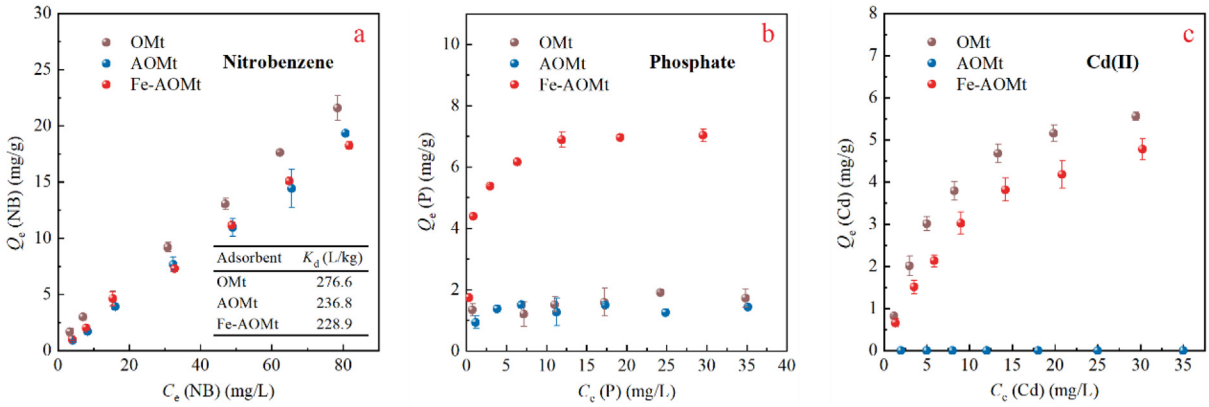

Fig. 4. Single-contaminant adsorption isotherms of OMt, AOMt and Fe-AOMt vs nitrobenzene (a), phosphate (b) and Cd(II) (c). The attached sheet in (a) offered the partition coefficient (K_d) of each adsorbent. The attached sheet in (a) offered the partition coefficient ($K_d = Q_e/C_e$) of each material. The experiment condition: temperature = 25 °C, pH = 4.00 ± 0.05, adsorbent dosage = 1 g/L.

existing with the preserved OMt layer. The PNS brought about total enhancement of pore structure, and favored the uniform loading of Fe hydroxides. Based on the preservation of hydrophobic interlayer spaces and effective loading of Fe hydroxides, we anticipate a promising co-adsorptive performance of Fe-AOMt towards HOCs, oxyanions contaminants and heavy metals.

3.2. Adsorptive performance

3.2.1. Adsorption isotherms of single contaminants

The adsorption isotherms of each single contaminants (i.e., nitrobenzene, phosphate, or Cd(II)) on OMt, AOMt and Fe-AOMt were provided (Fig. 4). The adsorption quantity of nitrobenzene (Q_e(NB)) on OMt was almost linearly correlated with its equilibrium concentration (C_e(NB)) in the solution, suggesting that partition effect should be the predominant sorption mechanism. It was suggested that intercalated surfactant cations with long alkyl chain such as $CTMA^+$ can form nano-sized hydrophobic media in the interlayer spaces of clay minerals, which could effectively uptake HOCs through a partition process (Zhu et al., 2009b, 2014a, 2016; Ma et al., 2016c); raw Mt usually showed rather weak affinity towards HOCs because of its hydrophilic interlayer spaces (Ma and Zhu, 2006; Zhu et al., 2009b, 2014a; Ma et al., 2016c). The capacity of organoclays for partitioning the HOCs is often quantified by the slope of the isotherms (Q_e/C_e), which is defined as partition coefficient (K_d). According to Fig. 4a, K_d of the three materials was in the following order: OMt (276.6 L/kg) > AOMt (236.8 L/kg) > Fe-AOMt (228.9 L/kg), showing that AOMt and Fe-AOMt retained most of the capacity of OMt towards nitrobenzene (AOMt retained 85.6% and Fe-AOMt retained 82.8%). These results were basically in agreement with the characterization results (XRD, FTIR, TEM and TOC analysis) that the intercalated $CTMA^+$ could keep most of its content during the acidification process of OMt and introduction of Fe hydroxides. On the other hand, the retaining of the capacity even after the introduction of Fe hydroxides made little loss to the K_d (Fig. 4a) and $CTMA^+$ content (Fig. S1a), implying that most of the Fe hydroxides may be supported in the external pores created by the acid activation rather than the interlayer spaces.

Adsorption isotherms of these materials towards phosphate in single-contaminant system were compared in Fig. 4b. In order to better understand the adsorption, Langmuir and Freundlich models were applied to fit the adsorption isotherms, and the former fits them better (Table S2); similar results were obtained for the surface adsorption onto many other adsorbents (Duman et al., 2015b, 2016, 2019; Fu et al., 2018; Ma et al., 2016c). The maximum adsorption capacity obtained from the Langmuir model for the three materials was in the following order: Fe-AOMt (~7.4 mg P/g) > AOMt (~2 mg P/g) ≈ OMt (~2 mg P/g). The poor performance of OMt and AOMt suggested that the Si–OH created in PNS in AOMt may not be able to adsorb phosphate. Some researches implied that Si–OH might adsorb phosphate through the hydrogen bonding, but no solid evidence was reported (Murashov and Leszczynski, 1999; Sabah and Majdan, 2009). The enhanced capacity of Fe-AOMt implied that there should be differences between the adsorption behaviors of Fe–OH and Si–OH. Previous studies have mentioned that hydroxyl groups on the solid surface of Fe hydroxides (denoted as ≡Fe–OH) can adsorb phosphate through ligand exchange by forming ≡Fe–P (Ma and Zhu, 2006; Zhu et al., 2014b; Liu et al., 2017). Similar behaviors on aluminum (hydr)oxides were also reported (Miyazaki et al., 1996; Kasama et al., 2004; Zhu et al., 2009b).

Different adsorption performances of these materials towards Cd(II) were observed (Fig. 4c): OMt was able to adsorb Cd(II), similar to raw Mt (Bhattacharyya and Gupta, 2008), while AOMt almost showed no affinity. After introduction of Fe hydroxides, the adsorption capacity of Cd(II) was recovered. Langmuir models fits the adsorption isotherms of Cd(II) better (Table S2). The adsorption capacity of OMt (Q_{max} ≈ 7.3 mg Cd(II)/g) can be attributed to the fact that some of its CEC was still occupied by original exchangeable cations (e.g., Ca^{2+}). The dramatical weakening of AOMt towards Cd(II) was probably due to the loss of available CEC and alteration of the surface charge. The recovery of the adsorption capacity of Fe-AOMt (Q_{max} ≈ 6.75 mg/g) may be contributed by the surface hydroxyl groups on the introduced Fe hydroxides (≡Fe–OH) could also release H^+ and adsorb Cd(II) through ligand exchange and form surface complexes (≡Fe–O–Cd) (Zhu et al., 2014b; Liu et al., 2017).

3.2.2. Performance in the multi-contaminant system

The adsorption performance of OMt, AOMt, and Fe-AOMt in single- and multiple-component system was compared where the initial concentration of each contaminant was constant (Fig. 5). The co-existence of phosphate and Cd(II) hardly made disturbance on the removal of nitrobenzene by all of the three adsorbents, due to the different adsorption sites they were attracted and distinct mechanisms mentioned in *section 3.1.1*. However, for the adsorption of phosphate and Cd(II), the behavior of Fe-AOMt differed from AOMt and OMt in the multiple-component system, as the synergetic effect between phosphate and Cd (II) was only detected on Fe-AOMt; for Fe-AOMt, the adsorption capacity of phosphate increased from ~7.6 to ~11.3 mg/g and that for Cd (II) rose from ~4.3 to ~9.0 mg/g. Similar trend was observed on other adsorbents with exposure of Fe–OH (Zhu et al., 2014b; Liu et al., 2017), even when some other oxyanions and cations were set as the adsorbates (Gräfe and Sparks, 2005; Liu et al., 2016a, 2016b). The synergetic effect will be further discussed in section 3.2.3 and 3.2.4 based on pH edge experiment and XPS patterns.

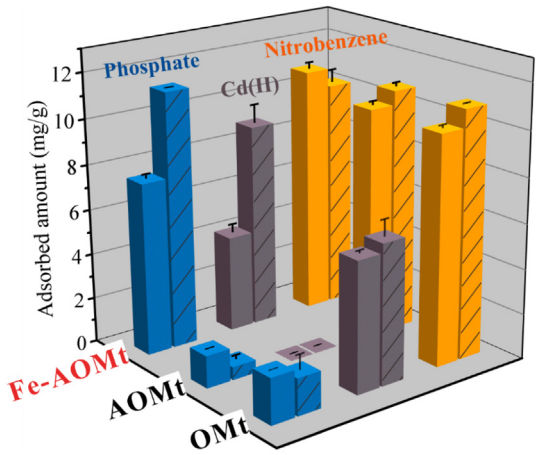

Fig. 5. Comparative adsorption of nitrobenzene, phosphate and Cd(II) on OMt, AOMt and Fe-AOMt in single- and multi-contaminant adsorption system. The performances in the multi-contaminant system are discriminated with dash lines on columns. The experiment condition: temperature = 25 °C, pH = 4.00 ± 0.05, adsorbent dosage = 1 g/L, initial concentration C_0(NB) = 60 mg/L and C_0(P) = C_0(Cd) = 25 mg/L.

3.2.3. Effect of pH

To investigate how solution pH influence the performance of Fe-AOMt, its effect on the removal of each contaminant in single- and multi-contaminant systems was examined (Fig. 6). In both systems, the performance towards nitrobenzene was stable in the given pH range, while a prominent pH-dependence of phosphate and Cd(II) adsorption on Fe-AOMt was observed.

Nitrobenzene can hardly ionize and therefore exists in form of molecule in aqueous solution. Electrostatic interaction and surface complexation, which are pH-dependent and usually need an ionic structure of adsorbate, can therefore contributed little to its sorption. The removal of nitrobenzene by OMt, AOMt and Fe-AOMt is based on partition, which is dominated by the hydrophobic media formed by intercalated surfactant as indicated in *section 3.2.1* and some literatures (Wang et al., 2010; Zhu et al., 2010; Zhu et al., 2015). Similar sorption process involved other non-ionizable HOCs was also reported to be pH-independent (Ma and Zhu, 2006).

The adsorption of phosphate in single- and multi-contaminant systems (Fig. 6b) was both negatively correlated with the equilibrium pH. As pH increased in the single-phosphate system, the surface charge of Fe-AOMt became less positive or more negative, which would weaken the electrostatic interaction between phosphate and Fe-AOMt (Antelo et al., 2010; Barthelemy et al., 2012). At the same time, increasing concentration of OH^- may enhance its competitiveness in the ligand exchange and therefore reduce the adsorption of phosphate (Dimirkou et al., 2009). Due to the synergetic effect, the removal of phosphate in the multi-contaminant system was enhanced in the detected pH range, compared to that in the single-phosphate system. The co-adsorption of Cd(II) also partly relieved the negative pH effect on phosphate, since the adsorption of Cd(II) was enhanced in increasing pH (Fig. 6c) and would then contribute to the adsorption of phosphate.

The effect of pH on Cd(II) in both systems was an inversion of that on phosphate: the increase of pH strongly favored the removal of Cd(II) (Fig. 6c). Such benefit can be ascribed to the change of electrostatic force and reduced competitiveness of H^+. In the multi-contaminant system, the adsorption of Cd(II) at different pH was also promoted due to the synergetic effect.

3.2.4. XPS evidence of (co-)adsorption mechanism

XPS have proven a useful tool to investigate the chemical environment and composition of surface elements (Zhu et al., 2014b; Ma et al., 2015; Liu et al., 2016a, 2016b; Chen et al., 2018). High-resolution XPS patterns of Fe-AOMt after adsorption in single- (containing phosphate / Cd(II)), binary- (containing nitrobenzene and phosphate / Cd(II)) and multi-contaminant systems (containing nitrobenzene, phosphate and Cd(II)) were obtained to investigate its adsorption mechanism (Fig. 7). The single peak in the range of binding energy from 126 to 143 eV is attributed to the P 2p of adsorbed phosphate on Fe-AOMt in each system (Fig. 7a). The P 2p peak in the "P" system (133.63 eV) did not obviously shifted in "NB + P" (133.63 eV) and "NB + P + Cd" system (133.68 eV), implying similar chemical environments for phosphorus in each system (Fig. 7a). This result suggests that phosphate was preferred than Cd(II) on the surface of Fe-AOMt and tend to dominate surface hydroxyl groups, forming P-bridged ternary surface complexes (≡Fe–P–Cd), as also indicated in other literatures (Zhu et al., 2014b; Ma et al., 2015).

The peaks in the range 394–418 eV should belong to Cd 3d and N 1 s, while some unexpected overlap may occur (Fig. 7b). The peaks at ~400.0 eV and ~402.9 eV in the three systems can be attributed to the nitrogen in $CTMA^+$ adsorbed in Fe-AOMt via two different mechanisms, respectively (Naranjo et al., 2013). The peaks at 406.16 eV, 406.15 eV and 405.89 eV in "Cd", "NB + Cd" and "NB + P + Cd" system respectively should be considered as a combination of Cd $3d_{3/2}$ from adsorbed Cd(II) and N 1 s from NO_3^- (indicated by FTIR patterns in Fig. 1b) and sorbed nitrobenzene (Kishi et al., 1979). It is therefore hard to discriminate the environment of adsorbed Cd(II) in different systems from Cd $3d_{3/2}$ peaks.

The peaks at 413.20 eV, 413.23 eV and 412.76 eV in "Cd", "NB + Cd" and "NB + P + Cd" system are attributed to the Cd $3d_{5/2}$,

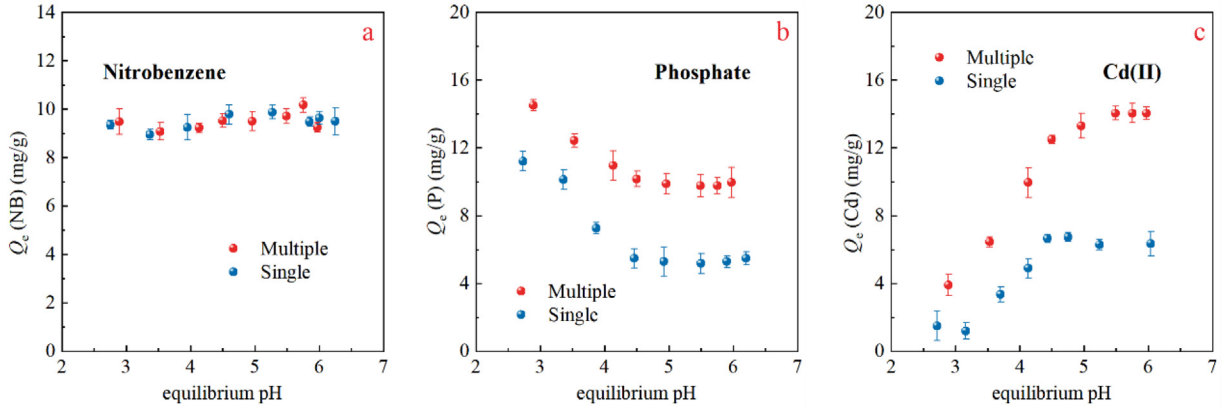

Fig. 6. pH effect on the adsorption of nitrobenzene (a), phosphate (b) and Cd(II) (c) on Fe-AOMt in single- and multi-contaminant system. The experiment condition: temperature = 25 °C, adsorbent dosage = 1 g/L, initial concentration C_0(NB) = 60 mg/L and C_0(P) = C_0(Cd) = 25 mg/L. Note that equilibrium pH, i.e., the pH at adsorption equilibrium, was set as the variable to better correspond to Q_e (adsorption quantity at the equilibrium).

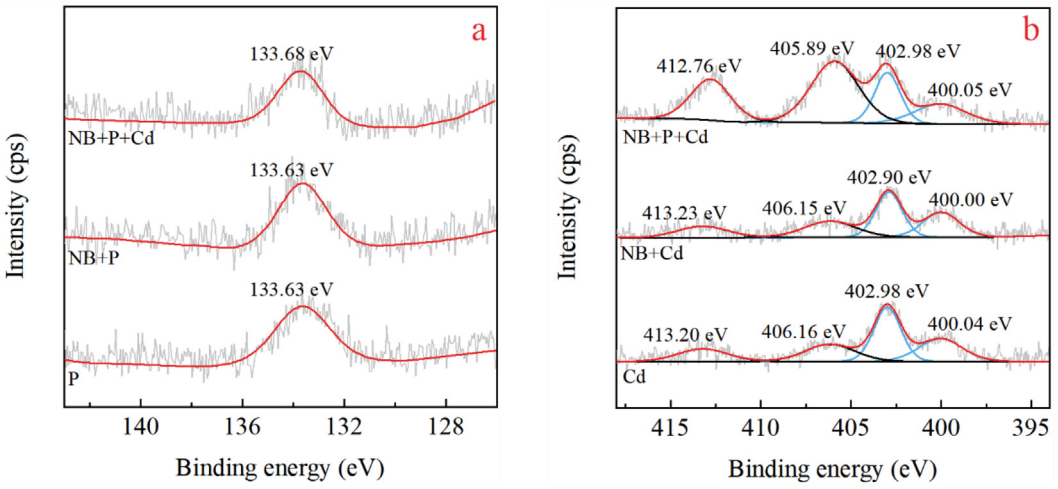

Fig. 7. XPS spectra of Fe-AOMt after the adsorption in systems containing different contaminants in the range 126–143 eV (a) and 394–418 eV (b).

which should not be interfered by any signal from N 1 s. As our previous work reported, the Cd 3d binding energy of adsorbed Cd(II) directly bonded to the solid surface should be much larger than that bonded with the adsorbed phosphate (Zhu et al., 2014b; Ma et al., 2015). These peaks revealed consistency with the previous work, that the Cd $3d_{5/2}$ of adsorbed Cd(II) in "NB + P + Cd" system (412.76 eV) was much lower than that in "Cd" and "NB + Cd" system, indicating obviously different environments of adsorbed Cd(II) in system containing phosphate and free of phosphate. Thus, one would expect that in the multi-contaminant system, Cd(II) was adsorbed by bonding to the adsorbed phosphate on Fe-AOMt (≡Fe–P–Cd) rather than directly to its surface (≡Fe–Cd).

As previous studies indicated, the synergetic effect between phosphate and Cd(II) on Fe hydroxides was mainly attributed to the formation of P-bridged ternary surface complexes (≡Fe–P–Cd); the bonded Cd could further adsorb phosphate, forming ≡Fe–P–Cd–P complexes (Zhu et al., 2014b; Liu et al., 2017). Formation of such complexes can provide additional adsorption sites for both phosphate and Cd(II). The formation of ternary surface complexes on Al–OH in multi-contaminant system was also reported (Li et al., 2013; Ma et al., 2016c). However, such synergetic effect was not observed on OMt and AOMt, because the affinity of OMt and AOMt towards phosphate was too weak to form stable chemical bond (mentioned in *section 3.1.1*), and therefore the P-bridge surface complexes could hardly form. On the other hand, our previous work has proposed that Cd-bridged surface complexes could also form in some cases (Liu et al., 2017). Although OMt showed some affinity towards Cd(II) in both system (Fig. 5), the absence of the synergetic effect suggested that neither P- or Cd-bridged surface complexes could form in this case, where Cd(II) was adsorbed through the cation exchange (as mentioned in *section 3.2.1*). It was reported that cation exchange could be even inhibited when co-existing phosphate appeared in relatively heavy concentration (e.g., up to 480 mg/L) due to the formation of anionic complexes in bulk solution (e.g., $[Cu(HPO_4)_2]^{2-}$ for Cu^{2+} and phosphate) (Inglezakis et al., 2003). Additionally, the poor performance of AOMt on phosphate and Cd(II) in the multiple-component system suggested again that surface Si–OH in the PNS possessed different adsorption behaviors from that of Fe–OH and Al–OH.

It was verified from the adsorption performance and detection by XPS that Mt was multi-functionalized successfully via our new strategy. Although some other clay mineral-based adsorbent has been synthesized to remove nitrobenzene, phosphate and Cd(II) from water (Table 2), simultaneous removal of these contaminants was seldom reported. On the other hand, the performance of Fe-AOMt in multi-contaminant system was even comparable with these clay mineral-based adsorbents, with respect to the removal of each single contaminant. Thus, Fe-AOMt was proved to be a novel and promising multifunctional adsorbent in wastewater treatment. Its performance was a good reflection of its structural composition, i.e., the uniformed distributed Fe hydroxides and the co-existing interlayer organic partition media. Moreover, the improved capacity was also contributed by the enhanced pore structure and specific surface area, which was considered to benefit the adsorption on nano-sized adsorbents in solutions (Khajeh et al., 2013).

4. Conclusion

A novel strategy to multi-functionalize Mt was developed and a new multifunctional adsorbent (Fe-AOMt) was then synthesized successfully. AOMt possessed PNS in its structure, featuring enhanced functional groups and pore structure, while most of the intercalated $CTMA^+$ could be preserved during the acidification. The introduced Fe hydroxides were able to be dispersed uniformly on AOMt. Accordingly, Fe-AOMt has proven effective on the simultaneous removal of nitrobenzene, phosphate and Cd(II). The synergetic effect between phosphate and Cd(II) on Fe-AOMt suggested the formation of ternary surface complexes (≡Fe–P–Cd), while the pH-independent uptake of nitrobenzene was hardly influenced by adsorption of phosphate and Cd (II), implying that the HOC and inorganic contaminants were adsorbed on different adsorptive sites with dissimilar mechanisms. Finally, XPS verified the formation of ternary surface complexes (≡Fe–P–Cd) in co-adsorption of phosphate and Cd(II) on Fe-AOMt. This work provided a new strategy to synthesize Mt-based multifunctional adsorbent, which was able to deal with HOCs, oxyanion contaminants and heavy metals simultaneously and effectively. In addition, the proposed new structure, where PNS and hydrophobic interlayer spaces co-exist, could offer clues to diversifying locations and types of active sites in materials based on layered clay minerals.

Acknowledgements

This work was financially supported by the National Key Research and Development Plan of China (2016YFD0800704), National Science Fund for Distinguished Young Scholars (41825003), National Natural Science Foundation of China (41572031, 41902040), Guangdong Special Support Program (2017TX04Z243), CAS Interdisciplinary Innovation Team (JCTD-2019-15), Youth Innovation Promotion Association CAS and Newton Advanced Fellowship (NA150190). The authors also thank Prof. Fei Ge from Xiangtan University for her valuable advice on promoting importance of this work, and Miss Zeyi Zeng

Table 2
Adsorption capacity of clay-mineral based materials for nitrobenzene, phosphate and Cd(II). The hyphen "-" means that the data is not indicated in literature.

Adsorbents	Adsorption capacity (mg/g)	pH	Concentration range (mg/L)	References
nitrobenzene				
CTMA-Bent	6.0	5.5	60	(Zhu and Zhu, 2007)
CTMA-Al_{10}-Bent	4.8	5.5	60	(Zhu and Zhu, 2007)
SB16–2.0	~8.4	7	~150	(Zhu et al., 2015)
T-23TMA-Mt	~10.5	–	~60	(Zhu et al., 2014a, 2014b, 2014c)
Fe-AOMt	10.15	4	60	This study
phosphate				
AlPMt-1.0	10.36	5	20–140	(Ma et al., 2015)
CTAB-Al_{10}-Bent	7.63	5.5	0–20	(Zhu and Zhu, 2007)
Fe-Bent	11.2	3	25–60	(Yan et al., 2010)
$C_{0.4}$-AlPMt	10.07	5	20–140	(Ma et al., 2016c)
S10-Fe-B	9.82	~2.5	0–12	(Ma and Zhu, 2006)
Fe-AOMt	11.32	4	0–35	This study
Cd(II)				
AlPMt-1.0	22.17	5	30–240	(Ma et al., 2015)
Fe-Mont	25.7	5	20–200	(Wu et al., 2009)
Al_{13}-PAAMts	18.30	6.5	~500	(Yan et al., 2008)
$C_{0.4}$-AlPMt	14.10	5	30–210	(Ma et al., 2015)
$C_{1.0}$-AlPMt	10.12	5	30–210	(Ma et al., 2015)
Fe-AOMt	9.03	4	0–35	This study

and Miss Ou Lan for their suggestions on the color scheme of illustrations. This is contribution No.IS-2790 from GIGCAS.

Declaration of Competing Interest

The authors declare that they have no known competing financial interests or personal relationships that could have appeared to influence the work reported in this paper.

Appendix A. Supplementary data

Supplementary data to this article can be found online at https://doi.org/10.1016/j.clay.2019.105420.

References

Antelo, J., Fiol, S., Perez, C., Marino, S., Arce, F., Gondar, D., Lopez, R., 2010. Analysis of phosphate adsorption onto ferrihydrite using the CD-MUSIC model. J. Colloid Interface Sci. 347, 112–119.

Barthelemy, K., Naille, S., Despas, C., Ruby, C., Mallet, M., 2012. Carbonated ferric green rust as a new material for efficient phosphate removal. J. Colloid Interface Sci. 384, 121–127.

Bergaya, F., Lagaly, G., 2013. General Introduction: Clays, Clay Minerals, and Clay Science, 1st ed. Elsevier Inc Developments in Clay Science.

Bhattacharyya, K.G., Gupta, S.S., 2008. Adsorption of a few heavy metals on natural and modified kaolinite and montmorillonite: a review. Adv. Colloid Interf. Sci. 140, 114–131.

Breen, C., Madejová, J., Komadel, P., 1995. Characterisation of moderately acid-treated, size-fractionated montmorillonites using IR and MAS NMR spectroscopy and thermal analysis. J. Mater. Chem. 5, 469–474.

Breen, C., Zahoor, F.D., Madejova, J., Komadel, P., 1997. Characterization and catalytic activity of acid-treated, size-fractionated smectites. J. Phys. Chem. B 101, 5324–5331.

Chen, Q., Zhu, R., Liu, S., Wu, D., Fu, H., Zhu, J., He, H., 2018. Self-templating synthesis of silicon nanorods from natural sepiolite for high-performance lithium-ion battery anodes. J. Mater. Chem. A 6, 6356–6362.

Chen, H., Yang, H., Xi, Y., 2019. Highly ordered and hexagonal mesoporous silica materials with large specific surface from natural rectorite mineral. Microporous Mesoporous Mater. 279, 53–60.

Cornell, R.M., Schwertmann, U., 2003. The Iron Oxides: Structure, Properties, Reactions, Occurrences and Uses, 2nd ed. Wiley-VCH Verlag GmbH & Co. KGaA, Weinheim.

Dimirkou, A., Ioannou, Z., Golia, E.E., Danalatos, N., Mitsios, I.K., 2009. Sorption of cadmium and arsenic by goethite and clinoptilolite. Commun. Soil Sci. Plant Anal. 40, 259–272.

Dou, J., Huang, Q., Huang, H., Gan, D., Chen, J., Deng, F., Wen, Y., Zhu, X., Zhang, X., Wei, Y., 2019. Mussel-inspired preparation of layered double hydroxides based polymer composites for removal of copper ions. J. Colloid Interface Sci. 533, 416–427.

Duman, O., Tunc, S., Polat, T.G., 2015a. Adsorptive removal of triarylmethane dye (Basic Red 9) from aqueous solution by sepiolite as effective and low-cost adsorbent. Microporous Mesoporous Mater. 210, 176–184.

Duman, O., Tunc, S., Polat, T.G., 2015b. Determination of adsorptive properties of expanded vermiculite for the removal of C. I. Basic Red 9 from aqueous solution: Kinetic, isotherm and thermodynamic studies. Appl. Clay Sci. 109, 22–32.

Duman, O., Tunc, S., Bozoglan, B.K., Polat, T.G., 2016. Removal of triphenylmethane and reactive azo dyes from aqueous solution by magnetic carbon nanotube-kappa-carrageenan-Fe_3O_4 nanocomposite. J. Alloys Compd. 687, 370–383.

Duman, O., Ozcan, C., Polat, T.G., Tunc, S., 2019. Carbon nanotube-based magnetic and non-magnetic adsorbents for the high-efficiency removal of diquat dibromide herbicide from water: OMWCNT, OMWCNT-Fe_3O_4 and OMWCNT-kappa-carrageenan-Fe_3O_4 nanocomposites. Environ. Pollut. 244, 723–732.

Fu, H., Yang, Y., Zhu, R., Liu, J., Usman, M., Chen, Q., He, H., 2018. Superior adsorption of phosphate by ferrihydrite-coated and lanthanum- decorated magnetite. J. Colloid Interface Sci. 530, 704–713.

Goh, K.H., Lim, T.T., Dong, Z., 2008. Application of layered double hydroxides for removal of oxyanions: a review. Water Res. 42, 1343–1368.

Gräfe, M., Sparks, D.L., 2005. Kinetics of zinc and arsenate co-sorption at the goethite-water interface. Geochim. Cosmochim. Acta 69, 4573–4595.

He, H., Zhou, Q., Martens, W.N., Kloprogge, T.J., Yuan, P., Xi, Y., Zhu, J., Frost, R.L., 2006. Microstructure of $HDTMA^+$-modified montmorillonite and its influence on sorption characteristics. Clay Clay Miner. 54, 689–696.

Huang, Q., Liu, M., Chen, J., Wan, Q., Tian, J., Huang, L., Jiang, R., Wen, Y., Zhang, X., Wei, Y., 2017. Facile preparation of MoS_2 based polymer composites via mussel inspired chemistry and their high efficiency for removal of organic dyes. Appl. Surf. Sci. 419, 35–44.

Inglezakis, V.J., Zorpas, A.A., Loizidou, M.D., Grigoropoulou, H.P., 2003. Simultaneous removal of metals Cu^{2+}, Fe^{3+} and Cr^{3+} with anions SO_4^{2-} and HPO_4^{2-} using clinoptilolite. Microporous Mesoporous Mater. 61, 167–171.

Ishii, R., Nakatsuji, M., Ooi, K., 2005. Preparation of highly porous silica nanocomposites from clay mineral: a new approach using pillaring method combined with selective leaching. Microporous Mesoporous Mater. 79, 111–119.

Kasama, T., Watanabe, Y., Yamada, H., Murakami, T., 2004. Sorption of phosphates on Al-pillared smectites and mica at acidic to neutral pH. Appl. Clay Sci. 25, 167–177.

Khajeh, M., Laurent, S., Dastafkan, K., 2013. Nanoadsorbents: classification, preparation, and applications (with emphasis on aqueous media). Chem. Rev. 113, 7728–7768.

Kishi, K., Chinomi, K., Inoue, Y., Ikeda, S., 1979. X-ray photoelectron spectroscopic study of the adsorption of benzene, pyridine, aniline, and nitrobenzene on evaporated nickel and iron. J. Catal. 60, 228–240.

Komadel, P., 2016. Acid activated clays: Materials in continuous demand. Appl. Clay Sci. 131, 84–99.

Komadel, P., Madejová, J., 2013. Acid Activation of Clay Minerals, 2nd ed. Developments in Clay Science, Elsevier Ltd.

Krupskaya, V., Zakusin, S., Tyupina, E., Dorzhieva, O., Zhukhlistov, A., Belousov, P., Timofeeva, M., 2017. Experimental study of montmorillonite structure and transformation of its properties under treatment with inorganic acid solutions. Minerals 7, 49.

Lei, Y., Cui, Y., Huang, Q., Dou, J., Gan, D., Deng, F., Liu, M., Li, X., Zhang, X., Wei, Y., 2019. Facile preparation of sulfonic groups functionalized Mxenes for efficient removal of methylene blue. Ceram. Int. 45, 17653–17661.

Li, W., Wang, Y.J., Zhu, M., Fan, T.T., Zhou, D.M., Phillips, B.L., Sparks, D.L., 2013. Inhibition mechanisms of Zn precipitation on aluminum oxide by glyphosate: a ^{31}P NMR and Zn EXAFS study. Environ. Sci. Technol. 47, 4211–4219.

Li, L., Qi, G., Wang, B., Yue, D., Wang, Y., Sato, T., 2018. Fulvic acid anchored layered double hydroxides: a multifunctional composite adsorbent for the removal of anionic dye and toxic metal. J. Hazard. Mater. 343, 19–28.

Liu, C., Wu, P., Zhu, Y., Tran, L., 2016a. Simultaneous adsorption of Cd(II) and BPA on amphoteric surfactant activated montmorillonite. Chemosphere 144, 1026–1032.

Liu, J., Zhu, R., Xu, T., Xu, Y., Ge, F., Xi, Y., Zhu, J., He, H., 2016b. Co-adsorption of phosphate and zinc(II) on the surface of ferrihydrite. Chemosphere 144, 1148–1155.
Liu, J., Zhu, R., Liang, X., Ma, L., Lin, X., Zhu, J., He, H., Parker, S.C., Molinari, M., 2017. Synergistic adsorption of Cd(II) with sulfate/phosphate on ferrihydrite: an in situ ATR-FTIR/2D-COS study. Chem. Geol. 477, 12–21.
Low, J., Cao, S., Yu, J., Wageh, S., 2014. Two-dimensional layered composite photocatalysts. Chem. Commun. 50, 10768–10777.
Ma, J., Zhu, L., 2006. Simultaneous sorption of phosphate and phenanthrene to inorgano-organo-bentonite from water. J. Hazard. Mater. 136, 982–988.
Ma, L., Zhu, J., Xi, Y., Zhu, R., He, H., Liang, X., Ayoko, G., 2015. Simultaneous adsorption of Cd(II) and phosphate on Al-13 pillared montmorillonite. RSC Adv. 5, 77227–77234.
Ma, L., Chen, Q., Zhu, J., Xi, Y., He, H., Zhu, R., Tao, Q., Ayoko, G.A., 2016a. Adsorption of phenol and Cu(II) onto cationic and zwitterionic surfactant modified montmorillonite in single and binary systems. Chem. Eng. J. 283, 880–888.
Ma, L., Xi, Y., He, H., Ayoko, G.A., Zhu, R., Zhu, J., 2016b. Efficiency of Fe-montmorillonite on the removal of Rhodamine B and hexavalent chromium from aqueous solution. Appl. Clay Sci. 120, 9–15.
Ma, L., Zhu, J., Xi, Y., Zhu, R., He, H., 2016c. Adsorption of phenol, phosphate and Cd(II) by inorganic-organic montmorillonites: a comparative study of single and multiple solute. Colloids Surf. A Physicochem. Eng. Asp. 497, 63–71.
Madejová, J., Bujdák, J., Janek, M., Komadel, P., 1998. Comparative FT-IR study of structural modifications during acid treatment of dioctahedral smectites and hectorite. Spectrochim. Acta - Part A Mol. Biomol. Spectrosc. 54, 1397–1406.
Madejová, J., Pálková, H., Pentrak, M., Komadel, P., 2009. Near-infrared spectroscopic analysis of acid-treated organo-clays. Clay Clay Miner. 57, 392–403.
Miyazaki, A., Matsuo, M., Tsurumi, M., 1996. Surface-complex formation between Zn ions and amorphous aluminosilicate in aquatic systems. J. Colloid Interface Sci. 177, 335–338.
Murashov, V., Leszczynski, J., 1999. Adsorption of the phosphate groups on silica hydroxyls: an ab initio study. J. Phys. Chem. A 103, 1228–1238.
Naranjo, P., Sham, E., Castellon, E., Sanchez, R., Torres, E., 2013. Identification and quantification of the interaction mechanisms between the cationic surfactant HDTMA-Br and montmorillonite. Clay Clay Miner. 61, 98–106.
Okada, K., Yoshizaki, H., Kameshima, Y., Nakajima, A., MacKenzie, K.J.D., 2010. Porous properties of mesoporous silicas from two silica sources (acid-leached kaolinite and Si-alkoxide). J. Porous. Mater. 17, 19–25.
Pálková, H., Madejová, J., Righi, D., 2003. Acid dissolution of reduced-charge Li- and Ni-montmorillonites. Clay Clay Miner. 51, 133–142.
Pentrák, M., Hronský, V., Pálková, H., Uhlík, P., Komadel, P., Madejová, J., 2018. Alteration of fine fraction of bentonite from Kopernica (Slovakia) under acid treatment: a combined XRD, FTIR, MAS NMR and AES study. Appl. Clay Sci. 163, 204–213.
Rahmi, Lelifajri, Nurfatimah, R., 2019. Preparation of polyethylene glycol diglycidyl ether (PEDGE) crosslinked chitosan/activated carbon composite film for Cd^{2+} removal. Carbohydr. Polym. 199, 499–505.
Sabah, E., Majdan, M., 2009. Removal of phosphorus from vegetable oil by acid-activated sepiolite. J. Food Eng. 91, 423–427.
Shen, Y., Chen, B., 2015. Sulfonated graphene nanosheets as a superb adsorbent for various environmental pollutants in water. Environ. Sci. Technol. 49, 7364–7372.
Steudel, A., Batenburg, L.F., Fischer, H.R., Weidler, P.G., Emmerich, K., 2009. Alteration of swelling clay minerals and magadiite by acid activation. Appl. Clay Sci. 44, 95–104.
Tang, J., Lv, H., Gong, Y., Huang, Y., 2015. Preparation and characterization of a novel graphene/biochar composite for aqueous phenanthrene and mercury removal. Bioresour. Technol. 196, 355–363.
Tkáč, I., Komadel, P., Müller, D., 1994. Acid-treated montmorillonites-a study by ^{29}Si and ^{27}Al MAS NMR. Clay Miner. 29, 11–19.
Tomić, Z.P., Ašanin, D., Antić-Mladenović, S., Poharc-Logar, V., Makreski, P., 2012. NIR and MIR spectroscopic characteristics of hydrophilic and hydrophobic bentonite treated with sulphuric acid. Vib. Spectrosc. 58, 95–103.
USEPA, 1983. Method 365.2, Methods for Chemical Analysis of Water and Wastes, 2nd ed. U.S. Environment Protection Agency.
Vicente Rodriguez, M.A., Gonzfilez, J. de D.L., Mufioz, M.A.B., 1995. Preparation of microporous solids by acid treatment of a saponite. Microporous Mater. 4, 251–264.
Wang, T., Zhu, J., Zhu, R., Ge, F., Yuan, P., He, H., 2010. Enhancing the sorption capacity of CTMA-bentonite by simultaneous intercalation of cationic polyacrylamide. J. Hazard. Mater. 178, 1078–1084.
Wang, L., Zang, L., Zhao, J., Wang, C., 2012. Green synthesis of shape-defined anatase TiO_2 nanocrystals wholly exposed with {001} and {100} facets. Chem. Commun. 11736–11738.
Wang, L., Wang, X., Cui, S., Fan, X., Zu, B., Wang, C., 2013. TiO_2 supported on silica nanolayers derived from vermiculite for efficient photocatalysis. Catal. Today 216, 95–103.
Wang, L., Wang, X., Yin, J., Wang, C., 2016. Insights into the physicochemical characteristics from vermiculite to silica nanosheets. Appl. Clay Sci. 132–133, 17–23.
Wang, L., Bahnemann, D., Bian, L., Dong, G., Zhao, J., Wang, C., 2019. Two-dimensional layered zinc silicate nanosheets with excellent photocatalytic performance for organic pollutant degradation and CO_2 conversion. Angew. Chemie. Int. Ed. 58, 8103–8108.
Wu, P., Wu, W., Li, S., Xing, N., Zhu, N., Li, P., Wu, J., Yang, C., Dang, Z., 2009. Removal of Cd^{2+} from aqueous solution by adsorption using Fe-montmorillonite. J. Hazard. Mater. 169, 824–830.
Yan, L., Shan, X., Wen, B., Owens, G., 2008. Adsorption of cadmium onto Al-13-pillared acid-activated montmorillonite. J. Hazard. Mater. 156, 499–508.
Yan, L., Xu, Y., Yu, H., Xin, X., Wei, Q., Du, B., 2010. Adsorption of phosphate from aqueous solution by hydroxy-aluminum, hydroxy-iron and hydroxy-iron-aluminum pillared bentonites. J. Hazard. Mater. 179, 244–250.
Yuan, P., Annabi-Bergaya, F., Tao, Q., Fan, M., Liu, Z., Zhu, J., He, H., Chen, T., 2008. A combined study by XRD, FTIR, TG and HRTEM on the structure of delaminated Fe-intercalated/pillared clay. J. Colloid Interface Sci. 324, 142–149.
Zhang, Q., Liu, R., Guo, J., Liu, B., Xiang, J., Tian, Y., Peng, Q., Zhou, A., 2014. Unique lead adsorption behavior of activated hydroxyl group in two-dimensional titanium carbide. J. Am. Chem. Soc. 136, 4113–4116.
Zhu, L., Zhu, R., 2007. Simultaneous sorption of organic compounds and phosphate to inorganic-organic bentonites from water. Sep. Purif. Technol. 54, 71–76.
Zhu, L., Zhu, R., Xu, L., Ruan, X., 2007. Influence of clay charge densities and surfactant loading amount on the microstructure of CTMA-montmorillonite hybrids. Colloids Surf. A Physicochem. Eng. Asp. 304, 41–48.
Zhu, R., Wang, T., Ge, F., Chen, W., You, Z., 2009a. Intercalation of both CTMAB and Al_{13} into montmorillonite. J. Colloid Interface Sci. 335, 77–83.
Zhu, R., Zhu, L., Zhu, J., Ge, F., Wang, T., 2009b. Sorption of naphthalene and phosphate to the CTMAB–Al_{13} intercalated bentonites. J. Hazard. Mater. J. 168, 1590–1594.
Zhu, R., Wang, T., Zhu, J., Ge, F., Yuan, P., He, H., 2010. Structural and sorptive characteristics of the cetyltrimethylammonium and polyacrylamide modified bentonite. Chem. Eng. J. 160, 220–225.
Zhu, R., Chen, Q., Liu, H., Ge, F., Zhu, L., Zhu, J., He, H., 2014a. Montmorillonite as a multifunctional adsorbent can simultaneously remove crystal violet, cetyltrimethylammonium, and 2-naphthol from water. Appl. Clay Sci. 88–89, 33–38.
Zhu, R., Li, M., Ge, F., Xu, Y., Zhu, J., He, H., 2014b. Co-sorption of CD and phosphate on the surface of a synthetic hydroxyiron-montmorillonite complex. Clay Clay Miner. 62, 79–88.
Zhu, R., Zhao, J., Ge, F., Zhu, L., Zhu, J., Tao, Q., He, H., 2014c. Restricting layer collapse enhances the adsorption capacity of reduced-charge organoclays. Appl. Clay Sci. 88–89, 73–77.
Zhu, J., Qing, Y., Ma, L., Zhu, R., He, H., 2015. The structure of montmorillonites modified with zwitterionic surfactants and their sorption ability. Mineral. Petrol. 109, 349–355.
Zhu, R., Chen, Q., Zhou, Q., Xi, Y., Zhu, J., He, H., 2016. Adsorbents based on montmorillonite for contaminant removal from water: a review. Appl. Clay Sci. 123, 239–258.